Journal of Materials Research and Technology 38 (2025) 503–516

Contents lists available at ScienceDirect

Journal of Materials Research and Technology

journal homepage: www.elsevier.com/locate/jmrt

Hybrid experimental–numerical study on nanoindentation response of dual-phase steels: From macroscale to atomic scale

M. Fesahat [a], M. Javidani [b], M. Soltanieh [a], M. Mahmoudi [a], H. Vafaeenezhad [c,*]

[a] School of Materials Science & Engineering, Iran University of Science and Technology, Tehran, Iran
[b] Department of Applied Science, University of Québec at Chicoutimi, Saguenay, QC, G7H 2B1, Canada
[c] Department of Materials Science and Engineering, Engineering Faculty, Ferdowsi University of Mashhad, Azadi Square, Mashhad, Iran

ARTICLE INFO

Handling Editor: SN Monteiro

Keywords:
Dual-phase steel
Nanoindentation
Heat treatment
Finite element analysis (FEA)
Molecular dynamics (MD)

ABSTRACT

In this study, the elastic and plastic behaviors of the ferrite and martensite phases of dual-phase (DP) steels were investigated using nanoindentation data and the related constitutive equations. First, hardness (H) and elastic modulus (E) were determined to derive the monotonic yield stress (σ_y) and Hollomon's parameter and then for work hardening exponent (K) and work hardening rate (n).Next, the results obtained by the nanomechanical approach implemented herein were validated using the semiquantitative data computed by numerical finite element analysis (FEA) and molecular dynamics (MD). The difference between plasticity of ferrite and martensite can be attributed ti the geometrically necessary dislocations (GNDs), which stimulate work hardening. The elastic and plastic data of both the phases were incorporated into FEA to simulate the load–displacement curves and the projected regions. In addition, the load–displacement curves of the ferrite and martensite phases and the hardness and Young's modulus determined by MD were in good agreement with the nanoindentation test and FEA results. The strain-rate sensitivity of ferrite, which exhibited a lower hardness and greater indentation depth, was 0.0985, whereas that of martensite was approximately 0.087. Furthermore, the TEM images proved the existence of GNDs at the ferrite–martensite interface and their role in cell formation in the ferrite zone and interphase region.

1. Introduction

Dual-phase (DP) steels represent a class of advanced ferrous alloys with composite-like microstructures. These alloys possess a soft ferrite phase, which imparts ductility, and a hard martensite phase that enhances the strength [1]. This synergistic integration of the mechanical properties distinguishes DP steels from conventional high-strength low-alloy steels, rendering them more suitable for engineering applications and automotive industry [2–4]. Additionally, DP steels are characterized by their low initial flow stress and rapid work hardening at low plastic strains, which are governed by the morphologies and volume fractions of the constituent phases [5]. Generally, the mechanical properties of dual-phase (DP) steels were corresponded with the volume fraction of martensite and its carbon content [4].

Numerous works have focused on correlating the flow properties of DP steels with their composite microstructures and the individual mechanical responses of ferrite and martensite [6]. The law of mixtures has been widely adopted for predicting the macroscale properties based on phase-specific characteristics [7]. For instance, Ghassemi-Armaki et al. [8] employed micro-pillar compression to demonstrate that martensite governs the early-stage plastic deformation and rapid work hardening in DP steels. Their study also revealed a 20 % increase in hardness of ferrite near the ferrite–martensite interfaces compared to the bulk regions [9]. Park et al. [10] established a linear correlation between the martensite volume fraction and the plastic stress at large strains; the deviations were attributed to the retained austenite. Zhang et al. [7] identified that dislocation pile-ups functioned as critical barriers to glissade dislocations and shifted strain localization from the ferrite to interphase regions. Recent advances include cyclic inter-critical annealing by Ding et al. [11], which yielded lamellar DP steels with tensile strengths exceeding 1 GPa and good elongation [12].

The roles of carbon content and martensite fraction were systematically investigated by Concepcion et al. [13]; the hardness and ultimate tensile strength increased proportionally with these parameters [14]. Jahanara et al.[15 [][][]explored the impact of thermomechanical processing on ferrite grain refinement and martensite distribution, and

* Corresponding author.
E-mail addresses: hossein.vafa@gmail.com, hvafaeinezhad@um.ac.ir (H. Vafaeenezhad).

https://doi.org/10.1016/j.jmrt.2025.07.133
Received 14 May 2025; Received in revised form 10 July 2025; Accepted 14 July 2025
Available online 17 July 2025

Wu et al. [16] highlighted the degradation in ductility and mechanical stability due to pre-strain and high strain rates. Collectively, these studies underscore the importance of precise phase-specific mechanical property determination for understanding the behavior of DP steels.

Conventional mechanical testing methods, such as uniaxial tension and compression, face limitations in probing the microscale phases owing to size and morphological constraints [17]. In this regard, nanoindentation is emerging as a powerful alternative as it enables the localized characterization of hardness, elastic modulus, yield stress, and work hardening exponents in multiphase systems such as Mg alloys [18], Co-based superalloys [17], Ni-based superalloys [19], metallic glasses [20], and Ti alloys [21]. The minimal sample requirements and geometric flexibility of this technique further enhance its applicability [22]. The integration with computational approaches, such as molecular dynamics (MD) and finite element analysis (FEA), expands its application scope to predicting the mechanical properties [23] and evolution of dislocation substructures [24].This study implements nanoindentation, FEA, and MD to investigate the elastoplastic behaviors of ferrite and martensite and the atomistic plasticity in DP steels. By correlating the experimental data with the results of numerical simulations, the paper provides insights into phase-specific deformation mechanisms and validates the proposed hybrid methodology for multiphase material characterization.

2. Materials and methods

2.1. Instrumental nanoindentation

A Hitachi High Tech.-EOS method elemental analyzer was used to determine the chemical composition of the starting ferrous material (DP steel) under study. The chemical composition of the steel, with a sheet geometry, is listed in Table 1. First, the low-carbon steel with the initial grain size of 75 μm was cold-rolled, which generated a microstructure composed primarily of ferrite and a little lined pearlite. The samples were normalized in an austenite area at 960 °C for 25 min to obtain a DP structure. Next, they were normalized at an intercritical annealing temperatures between AC_1 and AC_3, which was found as a appropriate technique to create dual phase steel [25], determined using Eqs. (1) and (2) (820 °C for 15 min) [26]. Finally, all the samples were quenched in a 10 wt% brine solution.

$$AC_1 = 751 - (16.3 \times \%C) - (27.5 \times \%Mn) - (5.5 \times \%Cu) - (5.9 \times \%Ni) + (34.9 \times \%Si) + (12.7 \times \%Cr) + (3.4 \times \%Mo) = 743.28\ (^{\circ}C) \quad \text{Eq. (1)}$$

$$AC_3 = 881 - (206 \times \%C) - (15 \times \%Mn) - (26.5 \times \%Cu) - (20.1 \times \%Ni) - (0.7 \times \%Cr) + (53.1 \times \%Si) + (41.7 \times \%V) = 850.36\ (^{\circ}C) \quad \text{Eq. (2)}$$

For further image analysis, the polished samples were chemically etched in a solution of $Na_2S_2O_5$(10 g) in distilled water (100 mL), forming a separate stable layer between the dark martensite and white ferrite sections. After the heat treatment, the DP microstructure was investigated by field-emission scanning electron microscopy (FESEM). Twenty optical micrographs were acquired at different locations to ensure randomness and accuracy of image data interpretation. Following this, a microstructural analysis was performed. A Hysitron Triboscope nanoindenter with a Berkovich tip mounted onto a multimode Atomic Force Microscope (AFM) was used for nanomechanical testing of the ferrite and martensite phases. Prior to the nanoindentation experiment, a holding fragment in the air was used to alter the thermal drift effect for each test. Using Berkovich tip, all the nanoindentation experiments were conducted at a thermal drift of less than approximately 0.005 $\frac{nm}{s}$. A uniaxial tension test was conducted at a strain rate of 0.01 s^{-1} and in compliance with other requirements specified in the ASTM E8M standard to elaborately evaluate the mechanical properties of the heat-treated DP steel.

Table 1
Chemical composition of the cast DP steel.

Element	C	Mn	Si	P	Ni	Cr	Cu
wt.%	0.082	0.4	0.06	0.005	0.2	0.4	0.25

2.2. Numerical FEA simulation of nanoindentation process

A 3D model was created to simulate the indentation process using a Berkovich tip on the phases of the heat-treated DP steel. The finite element method was implemented on the DEFORM 3D-V6.0 commercial software to determine the linear elastic and plastic flow properties of the DP steel via nanoindentation. The Berkovich indenter, chosen as the rigid penetrator, had the same area-to-depth function as the standard Berkovich tip. Fig. 1 illustrates the geometry of the Berkovich tip and the preprocessed calculation domain in the FEA.

The sample meshing implemented an appropriate linear element with reduced integration, as shown in Fig. 2. Because of the high-stress-sensitivity zones in the FEA model, biased mesh generation was applied to both the indenter and the sample. This approach ensured finer element sizes at the specimen–indenter interfaces and coarser element sizes in other regions, thus maintaining accuracy in the FEA formulation, particularly in the interaction zones between the tip and the sample. To minimize the stiffness of the terminal edges, the sample height was set to five times greater than the maximum indentation depth. The mechanical properties of the ferrite and martensite phases were incorporated into FEA package in the form of stress–strain curves, derived from the nanoindentation data (detailed in Section 3.3). The displacement ramp in FEA involved both loading and unloading of the indenter. During the loading, the indenter gradually approached the superficial zone of the sample with a force of up to 3000 μN at a consistent velocity, which provided the load–displacement curve history. During the unloading, the sample returned to its initial position at the same rate. This unloading simulation is crucial for verifying the numerical data with the experimental load–displacement results. The interactions between the indenter and the sample surface were modeled at a friction coefficient of approximately 0.2, thus ensuring a flawless interface from which neither component could get disconnected during the loading or unloading. Initially, the indenter tip was assumed to be sharp; later, a slight bend was incorporated into it. The mechanical boundary and initial conditions were applied along the centerline of the tip under the sample surface for proper movement and fixation in the perpendicular directions. To prevent excessive distortion in the FEA domain, the arbitrary Lagrangian–Eulerian (ALE) adaptive remeshing technique was employed in this model.

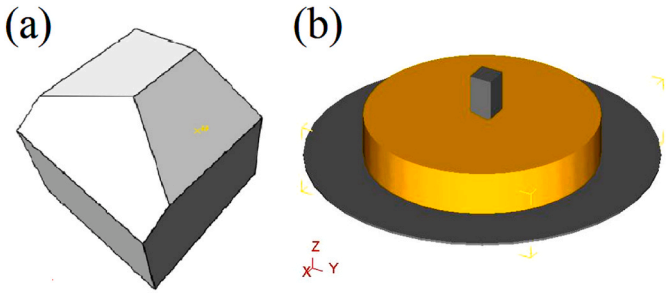

Fig. 1. (a) Sketch of the Berkovich tip used in this study and (b) the model assembled in the preprocessing step of the FEA.

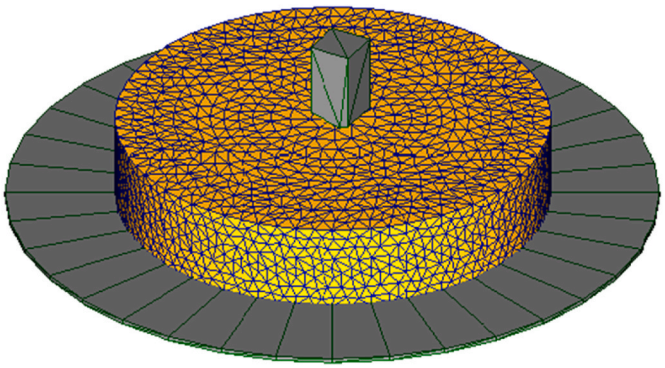

Fig. 2. Biased mesh generation for the elastic–plastic sample in contact with the Berkovich indenter.

2.3. Molecular dynamics simulation of the nanoindentation process

Fig. 3(a and b) shows the simulation models of the ferrite and martensite phases of the DP steel, in which the red atoms represent Fe atoms, and the blue atoms represent C atoms. The ferrite sample was modeled by including Fe and C atoms in the body-centered cubic crystal structure, with lattice parameter of 2.866 Å and the amount of C was set using the type/fraction command with random distribution of C in Fe. In contrast, the martensite sample was modeled by defining the unit cell of the body-centered tetragonal crystal structure, while BCT lattice was introduced to LAMMPS using custom lattice command and assigning Fe and C atoms to the specified positions. EAM/fs potential files, "*Fe_mm.eam.fs*"and "*Fe–C_Hepburn_Ackland.eam.fs*", were used to create a sample consisting of Fe and C atoms for both ferrite and martensite samples. The size of the ferrite sample was114 × 114 × 58 Å and that of the martensite sample was 86 × 86 × 44 Å, in the order of x-, y-, and z-directions. Periodic boundary conditions were assumed along all three dimensions, and1 fs was set as the time step for the simulations [27,28]. The energies of both the samples were minimized by applying the conjugate gradient algorithm for 1000 ps. A lattice parameter of 3.57 Å was considered to produce a rigid diamond indenter with a radius of 10 Å. Moreover, an indentation load was applied in the z-direction at a velocity of 0.1 $\left(\frac{\text{Å}}{\text{ps}}\right)$.To prevent atomic movements during the indentation using a rigid indenter, an 8 Å thick layer of boundary atoms at the bottom of both the samples was fixed. Furthermore, another 8 Å thick layer of thermostat atoms, maintained at a constant temperature of 300 K, was considered above the fixed layer. The remaining atoms were assumed as Newtonian layer atoms, which obey the classical Newton's second law. The NVE microcanonical ensemble was used in both the energy minimization and nanoindentation simulation steps, and the OVITO software was employed to visualize the atomistic configurations [27,28].

The embedded-atom method potential (eam/fs), which computes pairwise interactions in metals and metal alloys, was used for determining the interatomic potential between Fe and C in the ferrite and martensite samples based on Eq. (3), in which the total energy E_i of an atom I is calculated as follows [29]:

$$E_{-}(i) = F_{-}\left(\alpha\right)\ \left(\sum_{j\neq i}\rho_{\beta}\left(r_{i\,j}\right)\right) + \frac{1}{2}\sum_{j\neq i}\varphi_{\alpha\beta}\left(r_{i\,j}\right) \qquad \text{Eq. (3)}$$

where ρ, F, and φ are the density, a function of atomic electron density, and the pair potential interaction; α and β are the element types of atoms I and J, respectively. Moreover, as per the literature, interatomic interactions can be described using long-range van-der-Waals interactions, in the absence of chemical interactions between the atoms. Thus, the interatomic potential between the indenter atoms (C) and the Fe and C atoms in the ferrite and martensite substrates was modeled using the Lennard–Jones (lj) potential, according to Eq. (4) [30]:

$$E = 4\varepsilon\left[\left(\frac{\sigma}{r}\right)^{12} - \left(\frac{\sigma}{r}\right)^{6}\right]\ r\ <\ r_{-}(0) \qquad \text{Eq. (4)}$$

where r is the distance between two atoms; r_0, σ, and ε are potential parameters, which are constants with different values based on the interacting atomic species.

The lj potential coefficients used in this study are listed in Table 2.

3. Results and discussion

3.1. Microstructure and phase analysis of the DP steel

To confirm the presence of both the constituent phases, the peak positions of different plane indices were assessed in the X-ray diffraction (XRD) patterns. Owing to the relatively similar crystal structures of ferrite and martensite in the studied DP steel, their intensity versus diffraction angle patterns were often superimposed. For a clearer interpretation, the diffraction intensity of the (200) plane was deconvoluted using normal Gaussian bell-shape functions with different girths and peak locations. The Pseudo-Voigt calculation was employed on the Origin-lab commercial package software to deconvolute the overlapped peaks in the XRD spectra. Fig. 4 shows the results of fitting the superimposed (200) peaks after the intercritical annealing heat treatment. The widening of the peak indicates the presence of the martensite phase due to various crystal defects in its nonequilibrium lattice, whereas the narrowing of the peak represents the diffraction of the ferrite phase. The volume fractions of the martensite and ferrite phases were estimated by

Table 2
Lennard–Jones potential coefficients between different atoms used in this study.

Pair	σ (Å)	ε (eV)	Reference
Fe–C	2.2	0.0064	[31]
C–C	4.18	0.3050	[32]

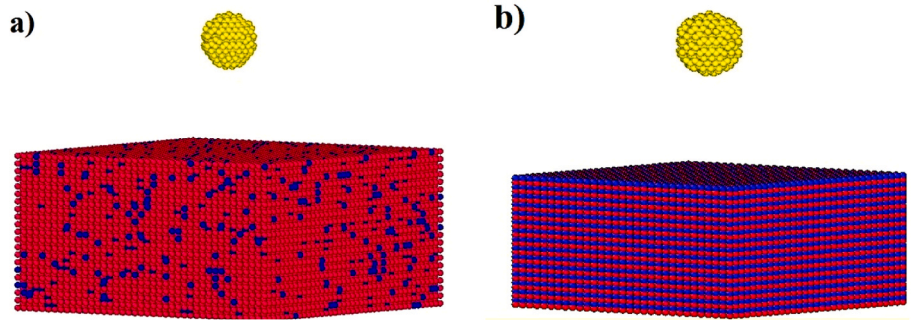

Fig. 3. MD models of the (a) ferrite sample and (b) martensite sample, containing Fe and C atoms.

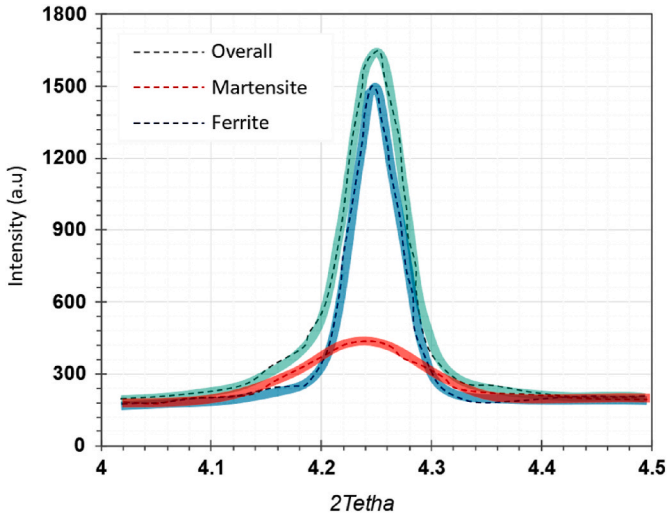

Fig. 4. XRD pattern of the DP steel after deconvoluting the peaks of the overall constituent phases.

the FESEM microstructural observations in Fig. 5.

Table 3 lists the volume fractions of the ferrite and martensite phases, determined by the quantitative XRD analysis and by the FESEM image analysis software (CELMEX) using the point count method according to ASTM E562. The results obtained from both the approaches demonstrated excellent consistency.

3.2. Nanomechanics of the constituent phases of DP steel

3.2.1. Evaluation of elastic and plastic characteristics

Nanoindentation experiments implement a two-phase loading–unloading cycle to achieve force-controlled indentation of the indenter into the sample. To evaluate the elastic and plastic flow characteristics, additional parameters such as the AFM-projected area and the slope of the unloading curve were factored in alongside the raw load–displacement data. Fig. 6 presents the loading–unloading curve, which includes the characteristic points used in the instrumental nanoindentation process.

According to Eq. (5), the load–displacement relationship of a Berkovich tip is expressed by a quadratic polynomial equation. In this equation, C represents the curvature of the graph, P is the applied load, and h denotes the indentation depth [33].

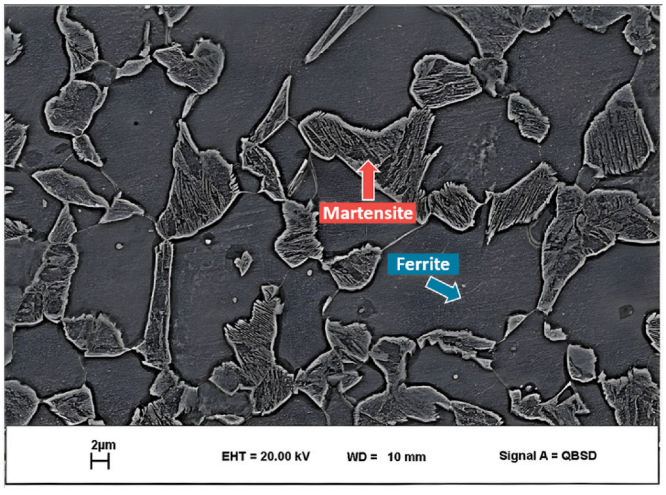

Fig. 5. SEM image of the heat-treated DP steel.

Table 3
Quantitative volume fractions of the ferrite and martensite phases.

Constituent phase of the DP steel	α	M
Image analysis	65 %	35 %

$$P = C \cdot h^2 \quad \text{Eq. (5)}$$

The hardness of the sample was determined using Eq. (6), which incorporates the time-dependent load history and the indented area (A_{max}) at maximum load level (P_{max}) during the contact [34]:

$$Hardness(H) = P_{max}/A_{max} \quad \text{Eq. (6)}$$

The key parameters from the instrumental nanoindentation test—the maximum depth (h_m), residual depth (h_r), curvature of the graph (C), and slope of the unloading curve (S_m)—are used to determine the elastic and plastic characteristics of a material, as outlined in Eq. (7). When the material is assumed to behave as a rigid plastic throughout the deformation regime, the yield stress (YS) is approximately one-third of the hardness determined from the nanoindentation test.

To model the plastic flow more accurately, the incremental variation in the yield stress (YS) must be considered because the elastic behavior of metallic materials is related to the Young's modulus, hardness, and tip angle (β), as displayed in Eq. (8).Accordingly, the hardness is correlated with the yield stress (YS) through a phenomenological relation (ψ),as shown in Eq. (8) [34]:

$$E = \frac{1}{c \cdot \sqrt{A_m}} \cdot \left[\frac{dP}{dh}\right]_{h=h_m} \quad \text{Eq. (7)}$$

$$\frac{H}{YS} = \Psi \cdot \left[\frac{E \cdot \beta}{YS}\right] \quad \text{Eq. (8)}$$

Johnson et al. implemented Eq. (9) to extract the elastic data of incompressible materials subjected to compression strain by a sharp-tipped indenter. The yield stress (YS) can be determined from the computed hardness (H) and Young's modulus (E) values [34].

$$\frac{H}{YS} = 0.45 \cdot \left[1 + \ln\left(\left(\frac{4YS}{3\pi E}\right) \cdot \tan\beta\right)\right] \quad \text{Eq. (9)}$$

When the elastic limit is surpassed and yielding occurs, plastic deformation is initiated, and work hardening becomes the dominant mechanism because of dislocation movements and interactions. Quantitatively, work hardening is proportional to the dislocation density. New dislocations can form near Frank–Reed sources, adding to the movement and interactions of existing dislocations. At the macroscale, work hardening is fundamentally defined as the increase in applied stress with increasing strain and can be expressed using various formulae. In general, there are two main classes of constitutive descriptions for work hardening.

When the elastic limit is surpassed and plastic deformation is initiated, dislocation slip and entanglement occur, manifesting as work hardening in the flow stress curve. Because the entangled dislocation networks prevent the movement of dislocations, and lead to difficult dislocations glide through the crystal lattice. This entanglement mechanism which gradually rises internal resistance within the alloy is a crucial contributor to work hardening [35]. In addition to the glide of perfect dislocations, the partial dislocations from Frank–Reed sources introduce additional deformation barriers and can lead to dislocation recombination. As mentioned earlier, work hardening is characterized by an increase in plastic stress with increasing strain and can be formulated using various classical equations. The Hollomon equation employs the power law to correlate plastic strain with stress, whereas the Ludwik equation correlates stress with both yield stress and plastic strain. In the Ludwik equation, an increase in yield stress indicates that the material was previously subjected to plastic strain. Since the DP steel

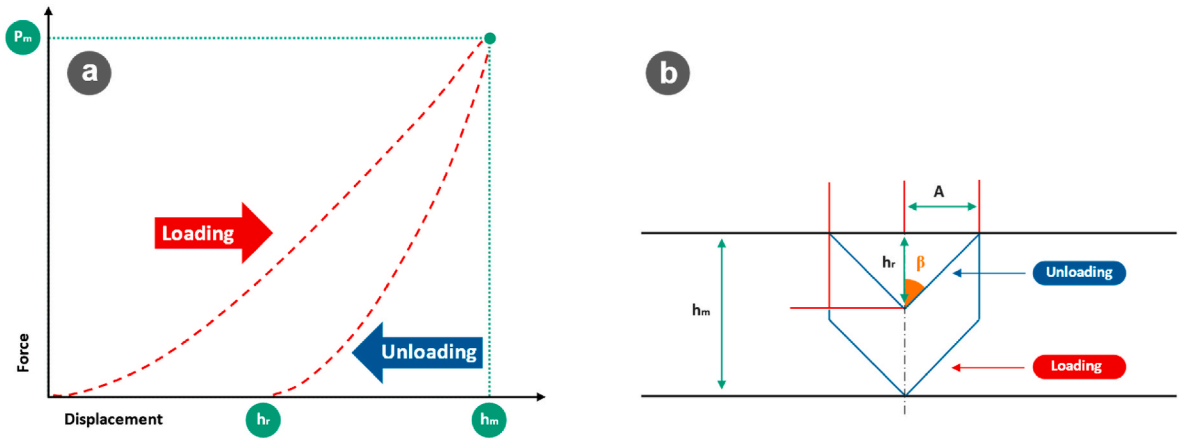

Fig. 6. Characteristic points of the nanoindentation test used for evaluating the elastic and plastic mechanical characteristics.

studied herein did not exhibit pre-strain, the Hollomon equation was applied in this nanomechanical investigation to define the work hardening (Eq. (10)).

$$\sigma = K \cdot \varepsilon^n \quad \text{Eq. (10)}$$

Here, n and K denote the work hardening exponent and work hardening rate, respectively. At the onset of yielding, the elastic stress equals the plastic flow stress calculated using the linear elastic relationship for Hookean materials, $\sigma = E\varepsilon$, as stated in Eq. (11):

$$YS = K \cdot \varepsilon_Y^n = E \cdot \varepsilon \quad \text{Eq. (11)}$$

The graph curvature is typically expressed using the elastic modulus and an analytical function that incorporates the work hardening exponent, yield stress, and tip angle, as shown in Eq. (12) [34]:

$$C = E_r \cdot F \cdot \left(\left(\frac{YS}{\overline{E}} \right), n, \beta \right) \quad \text{Eq. (12)}$$

Here, F is a function that correlates the curvature with both the elastic and plastic components. The reduced elastic modulus, E_r, specified in Eq. (13) is used as an alternative parameter for calculating E and for verification. However, in this study, Eq. (7) was employed instead of Eq. (13) [34].

$$E_r = \left[\left(\frac{1-\nu^2}{E} \right) + \left(\frac{1-\nu_i^2}{E_i} \right) \right]^{-1} \quad \text{Eq. (13)}$$

In this equation, ν_i and E_i are the elasticity parameters of the indenter; ν and E denote the Poisson's ratio and elastic modulus of the sample, respectively. However, Eq. (13) has inherent flaws because it employs elastic material factors to compute the work hardening rate. To address this drawback, the parameter σ_r (where subscript r denotes the residual indentation depth) was proposed for sharp tips; it is independent of β, as shown in Eq. (14). In the calculations used in instrumental nanoindentation data, σ_r denotes the stress equivalent to the pressure required to achieve pre-strain [34].

$$C = \sigma_r \cdot \widehat{F} \cdot (\sigma_r, n) \quad \text{Eq. (14)}$$

In the nanoscale domain of nanoindentation testing, the elasticity and instantaneous work hardening cumulatively govern the work hardening rate of the sample. Therefore, applying a function $\widehat{F}$ that considers the elastoplastic behavior enhances the computational accuracy, as represented by Eq. (15) [34]:

$$C = \sigma_r \cdot \widehat{F} \cdot \left[\left(\frac{\overline{E}}{\sigma_r} \right), \left(\frac{YS}{\sigma_r} \right) \right] \quad \text{Eq. (15)}$$

According to previous numerical and experimental studies [31–34], the function $\widehat{F}$ is the most accurate and comprehensive correlation factor for the elastoplastic data derived from the nanoindentation graph curvature (Eq. (16)). [34]:

$$C = \frac{P}{h^2} = [A.\sigma_{0.29}] \cdot \left[1 + \frac{YS}{\sigma_{0.29}} \right] \cdot \left[B + \ln \left(\frac{\overline{E}}{YS} \right) \right] \quad \text{Eq. (16)}$$

The constants A and B were determined through iterative trial-and-error estimations for various indenter tip geometries (see Table 4). $\sigma_{0.29}$ is an important parameter that merits careful consideration; it represents the stress corresponding to a specific strain of $\varepsilon_r = 0.29$ for the material under deformation. Numerical and experimental analyses using the Berkovich indenter have established that this value is applicable to both metals and ceramics [35,36]. According to the modeling approach proposed by Dao et al. [37], elastic properties can be expressed in terms of the unloading force (P_u) and the slope (S_u) of the load–displacement curve. Based on their geometric equations, the slope of the unloading phase can be mathematically described by Eq. (17) [34]:

$$S_u = \frac{dP_u}{dh} = \overline{E} \cdot h_m \cdot C \cdot \sqrt{\frac{A_m}{h_m}} \quad \text{Eq. (17)}$$

Here, C is a specific constant that defines the characteristic features of the indenter tip geometry. Its value for the Berkovich indenter is provided in Table 4.

Therefore, the work hardening exponent, n, of the plastic region can be estimated using two stress levels, $\sigma_{0.29}$ and the yield stress (YS), based on Eq. (25). Subsequently, the strength coefficient, K, can be determined using Eq. (10).

$$n = \frac{\ln \sigma_{0.29} - \ln YS}{\ln \sigma_{0.29} - \ln \varepsilon_{YS}} \quad \text{Eq. (18)}$$

Fig. 7 presents the load–displacement curves of the constituent phases, namely, soft ferrite and hard martensite. The fitting constant of the nanoindentation data, C, was determined by nonlinear curve fitting using Eq. (5) as the fitted function. To evaluate the plastic stress level, $\sigma_{0.29}$, Eq. (16) was solved algebraically using a graphical method. Finally, Eq. (18) was used to determine the work hardening rate, K, after calculating the n-value and the yield strain. The elastoplastic properties of ferrite and martensite were extracted from the previously mentioned numerical analysis of the nanoindentation test data and are presented in Table 4. The calculated true stress-strain curves for both phases are

Table 4
Characteristic tip geometry factors of the Berkovich indenter [36].

Constant	A	B	C
Value	6.02	−0.875	1.2370

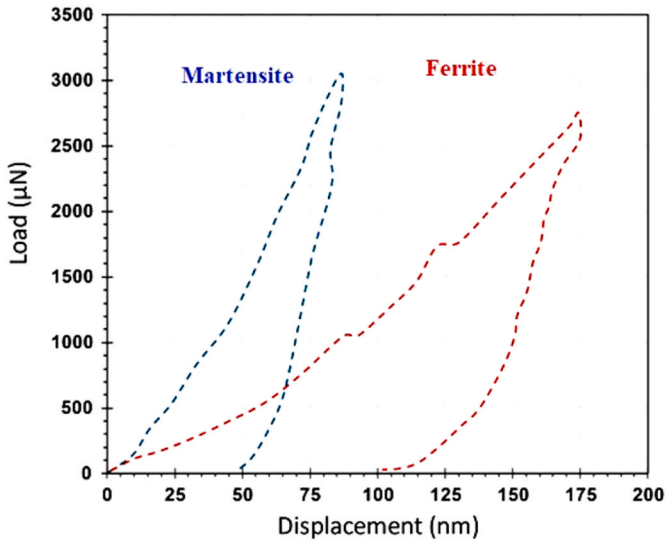

Fig. 7. Load–displacement curves of the constituent phases of the DP steel.

shown in Fig. 8. Moreover, the load–displacement curves of both the constituent phases (Fig. 7) exhibited pop-ins, indicating transition from the elastic to plastic region. The similarity of the graphs before the pop-in suggests that both the phases exhibited the same elastic properties.

For the calculations involving Eq. (13), the Young's modulus and the Poisson's ratio of the diamond-like indenter were assumed as 1141 GPa and 0.11 [37], respectively, and a Poisson's ratio of 0.3 was assumed for both the studied phases. The extracted Young's modulus values of ferrite and martensite were in good agreement with the results reported in other works on this composite-like structured material [38,39]. Moreover, by applying the equation $\sigma = \sigma\alpha \times f\alpha + \sigma m \times fm$, which is suitable for calculating σ of composite materials, the calculated yield stress (YS) of DP steel from ferrite and martensite yield stress [4] is 905.95 Mpa, which agreed well with the value in Table 5, (919 Mpa). Considering the mean volume fractions of each phase from Table 3, the error is approximately 1.5 %. It should be considered that the tensile properties of DP steels depend on the martensite volume and morphology, and it can be notably different even for the same chemical composition, which is well documented in literature [14,25,35].

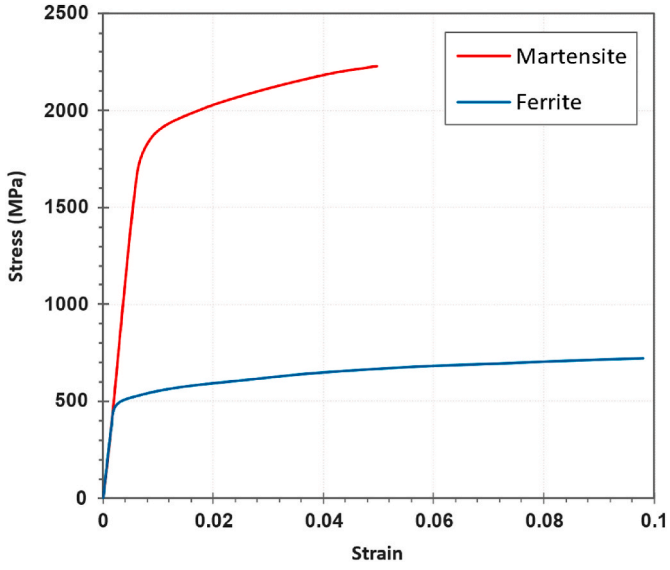

Fig. 8. True stress–strain curves of the ferrite and martensite phases determined by instrumental nanoindentation tests, based on the calculated data.

Table 5
Elastic and plastic mechanical properties of the ferrite and martensite phases (extracted from the nanoindentation test) and the DP steel samples (extracted from the tension test).

Constituent or overall phase	Ferrite	Martensite	DP steel
E(GPa)	206	207	–
H(GPa)	7.30	9.20	–
C(GPa)	125	216	–
YS(MPa)	473	1710	919
Tensile strength (MPa)	–	–	1292
ε_y	0.0023	0.009	0.0043
N	0.112	0.106	0.212
K(MPa)	934	3069	2428

The core objective of this research methodology is to redefine the plastic deformation of DP steel by considering the combined effect of its phases and the individual work hardening of ferrite and martensite. This was achieved by performing comprehensive calculations and analyzing the nanoindentation raw data, which revealed substantial differences between the plastic deformation behaviors of martensite and ferrite. The yield stress of ferrite was lower than that of the DP steel, whereas that of the martensite phase was higher. Additionally, the work hardening exponent of the DP steel lied between those of martensite and ferrite. This difference between the *n*-values reflects the ability of the steel to deform uniformly owing to its composite-like structure. Additionally, the results indicated that DP steels with a martensite volume fraction (V_m) of less than or equal to 50 % exhibited single-stage work hardening behavior and a linear ln δ–ln ε relation, signifying that the *n*-value remained constant during the deformation. Plastic deformation was initiated in ferrite and then progressed to martensite, collectively influencing the *n*-value of the DP steel under tension test at the macroscale. Initially, the plastic strain was predominantly concentrated in ferrite, and a small strain was dispersed in martensite during the deformation. The mechanical properties of each indented phase were determined by performing nanoindentation on the spots within that phase. The calculated yield stress and work hardening exponent for martensite were 805 MPa and 0.177, respectively, and 226 MPa and 0.253 for ferrite, in order. The corresponding values were determined from the macroscale tension experiments as 403 MPa and 0.212, indicating that the flow curves of martensite and ferrite lied above and below that of the DP steel, respectively. The results of this study were in good agreement with the data reported for martensite. However, some discrepancies were observed for ferrite, which can be attributed to the differences in chemical composition, ferrite size, and morphology of the surrounding martensite. Since the martensite phase of the DP steel exhibited a network morphology, the tensile properties (yield and tensile stresses) of the DP steel were poorer than those of martensitic steels with lath planes, which accommodate more dislocations and store a higher energy within their structures. Furthermore, the strain hardening—usually determined from the stress relationship index ($R_m/Rp_{0.2}$ or tensile strength/yield strength)—was calculated to be as high as 1.68 in this study, which is typical of DP steels and concurs with the values obtained in previous studies. Hence, for DP steels with different martensite alignments, their corresponding constitutive equations differ, which is worth exploring in future studies.

In addition, a higher hardness ratio signifies greater strength variations and strain incompatibility between the adjacent ferrite and martensite phases, leading to strain localization at the interphase boundaries, which in turn results in a higher crack density and void formation during the plastic deformation. Therefore, ahigh martensite: ferrite hardness ratio leads to reduced elongation, area reduction, and fracture toughness in the heat-treated steel.

The serrations in the stress–strain curves plotted from the nanoindentation data are attributed to the nucleation of discrete shear bands accommodating the plastic strain during the incremental penetration of the indenter tip. This phenomenon causes load reduction like

displacement burst or a pop-ins, as observed in the nanoindentation experiments. The formation of such serrated flows, which is indicative of shear band development, is partially influenced by the morphologies of adjacent phases at the interfaces. When the indenter tip penetrates ferrite, deformation bands are formed via continuous rotation of the crystal lattice, generating dislocations in the exposed phase. The movement and entanglement of these dislocations lead to strain buildup. In alloys with hard martensite networks, when deformation bands collide with the neighboring martensite structures, the complex atomic stacking of martensite delays the progression of these bands. Any obstruction to the dislocation movement increases the strain incompatibility at the ferrite–martensite interface, consequently increasing the difference in work hardening between the martensite bands and adjacent ferrite. This mechanism explains the formation of deformation bands with relatively large rotation angles at the ferrite–martensite interfaces, as proposed in previous studies on multiphase steels [6–8,13].

The strain hardenability of DP steels improves when martensite grains form a network structure around the ferrite grains. Although the strain hardenability gets significantly enhanced because of the increased tensile strain during the deformation, without any substantial elongation loss, the necking deformability gets reduced drastically. Moreover, the connecting regions of martensite grains serve as preferential sites for micro-void formation, and the number of micro-voids rapidly increases with the tensile strain, further decreasing the necking deformability. Fundamentally, the martensite grains in the DP structure function as a strengthener because martensite is much stronger than ferrite. Consequently, the ferrite matrix bears the plastic strain during the deformation, thereby generating discontinuous strain gaps and micro-voids at the ferrite–martensite interface [35]. To optimize strain partitioning between ferrite and martensite, which governs the strain hardening and the ductile fracture behavior of DP steels, Park et al. investigated the effects of martensite distribution and ferrite grain size [10]. A decrease in the ferrite grain size increases both the yield strength and tensile strength of the DP steel by nearly the same amount, indicating that ferrite grain refinement does not significantly affect strain hardening. In contrast, altering the martensite distribution from isolated to chained configurations increases the tensile strength and yield strength by different amounts. Their study reveals that while the increase in yield strength is relatively small, the tensile strength gets significantly enhanced, thus steepening the slope of the stress–strain curve and correspondingly increasing the strain hardening rate and work hardening of the DP steel. Generally, the strain partitioning between the ferrite and martensite phases in DP steels correlates with the volume fraction and morphology of the hard phase, and the flow characteristics of the individual phases [4,35,37]. When ferrite grains are enclosed within a martensite network, the slip deformation and dislocation movement in ferrite get restricted, causing significant strain partitioning into martensite and enhances martensite deformation. As a result, the average strain in the martensite region increases substantially during tensile deformation, reducing the strain partitioning between ferrite and martensite. Because martensite serves as a strengthener in the DP steel, a higher strain in the martensite region leads to better strain hardenability.

3.2.2. *Fracture toughness and plasticity criteria of ferrite and martensite*

During nanoindentation, radial cracks were formed in regions around the indentation zone when the indenter penetrated the material. The applied force and the crack length exhibited a definite relationship, as illustrated in Fig. 9. Analysis of these radial cracks, which initially nucleate beneath the indentation dimple, is the most conventional method for estimating fracture toughness, referred to as indent-crack fracture mechanics [38]. In this geometric analysis, the fracture toughness (K_{IC}) is expressed using Eq. (19) [38]:

$$K_{Ic} = \xi \cdot \left[C \cdot tan\left(\frac{\beta}{2}\right)\right]^{\frac{2}{3}} \cdot \left[\frac{E_r}{H}\right]^{\frac{1}{2}} \cdot \left[\frac{P}{C^{1.5}}\right] \forall \left\{\frac{c}{a} \gg 1\right\} \quad \text{Eq. (19)}$$

Here, ξ is an experimentally determined factor whose value is 0.032; P is the applied load; c and a represent the radial crack length and the contact size, respectively (Fig. 9). Cracks get initiated at the indenter tip when the induced stress at the crack tip is in equilibrium with the fracture toughness of the material, K_{IC}. Eq. (19) offers greater accuracy and repeatability for crack formation and propagation beneath symmetric indenters such as cubic corners and Vickers types. However, the asymmetrical geometry of the Berkovich tip could introduce errors in the calculations. Despite this constraint, the unique shape of the Berkovich tip facilitates mean the pyramidal geometry to converge into a specific zone rather than generating a concentrated trace, which is typical of sharp tips such as the Vickers. Therefore, Eq. (20) was used for calculating K_{IC}.

In the alternative formula that employs maximum load, K_{IC} can be represented as follows [38]:

$$K_{Ic} = 0.015 \times \sqrt{\frac{a}{l}} \cdot \left[\frac{E}{H}\right]^{2/3} \cdot \left[\frac{P_m}{C^{2/3}}\right] \quad \text{Eq. (20)}$$

Using both the formulae, the K_{IC} values of the ferrite and martensite phases were calculated and are presented in Table 6. The results reveal that martensite exhibited a lower crack resistance than ferrite, underscoring the influence of the martensite network morphology and the volume fraction formed during the heat treatment on the microstructure. But it should be mentioned that the formation of sub-cell in ferrite grains does not depend on the martensite volume fraction, and it was

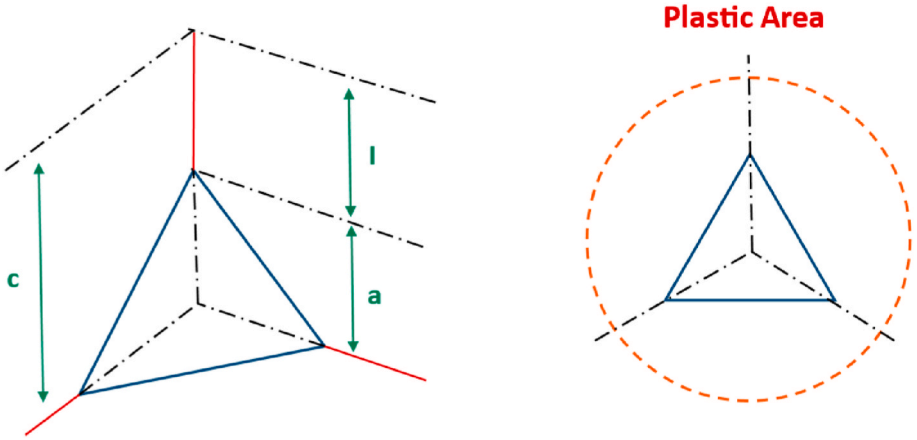

Fig. 9. Parameters used for calculating K_{IC} in the nanoindentation test.

Table 6
Fracture toughness (Mode I) of both the phases calculated using A and L methods.

Constituent phase of the DP steel	K_{IC} [MPa ($m^{0.5}$)] (sharp tip)	K_{IC} [MPa ($m^{0.5}$)] (asymmetrical tip)
Ferrite	21.5	17.6
Martensite	10.3	8.2

suggested in previous research that the cyclic softening behavior in DP steels is due to cell formation and martensite softening [37]. Additionally, the enhanced fracture toughness of the ferrite phase is attributed to toughening mechanisms such as crack healing via bridge formation along the crack boundaries, which increase the energy required for subsequent crack propagation.

To assess the toughness from the nanoindentation data, the brittleness parameter (BP) is used, as defined in Eq. (21) [39]:

$$PB = \left(\frac{H}{K_{IC}}\right) \quad \text{Eq. (21)}$$

Table 6 lists the brittleness properties of both the phases. The observed phenomena are possible correlated with their fracture toughness and crystal structures, which induce brittleness. This opens new research avenues for determining the most effective approach for this category of multiphase steels. Atomistic simulations and micro-computed tomography would be instrumental in advancing the understanding of this topic. Fig. 11displays the AFM maps of ferrite and martensite, obtained from the nanoindentation tests. These AFM images were used for calculating K_{IC}, establishing the ductility criteria, and validating the FEA data, as detailed in Section 3.2.3. Owing to their plastic deformation, the ductility of the ferrite and martensite phases can be assessed using the plasticity index (ξ), as defined in Eq. (22) [36]:

$$\xi = \frac{A_1}{A_1 + A_2} \quad \text{Eq. (22)}$$

Here, A_1 and A_2 denote the areas of the plastic and recovered (elastic) sections, respectively. The overarching criteria are $A_2 = 0$ (i.e., $\xi = 1$), indicating perfect plastic deformation without elasticity, and $A_1 = 0$ (i.e., $\xi = 0$), signifying perfect elastic deformation without plasticity. In practical scenarios, wherein $0<\xi < 1$, deformation follows an elastoplastic pattern. The areas can be evaluated through image analysis of both the loading and unloading curves, thus enabling the calculation of the plasticity index, ξ. As presented in Table 7, the ξ value of martensite was lower, implying reduced plastic deformation. In contrast, the ξ value of ferrite was higher (approximately 0.54), which indicates its ability to undergo increased plastic deformation. Furthermore, the exterior zones of both the phases exhibited pile-up effects, suggesting that both ferrite and martensite could accommodate certain levels of plastic deformation. This behavior is influenced by their anisotropic crystal structures, which contribute to considerable anisotropy in their mechanical responses.

In nanoindentation testing, work hardening can cause the regions around the indentation to exhibit either piling-up or sinking-in behavior. Pile-up occurs when a material accumulates around the indented spot and forms a raised rim, whereas sink-in occurs when the surface is depressed below its original level. To interpret these phenomena, we used Eq. (23), which employs the ratio of the indented area at a certain load (A_c) to the area at a higher load (A_g). A pile-up: sink-in ratio (PS) of greater than one indicates piling-up behavior, whereas a value less than one suggests sinking-in behavior [18,40].

Table 7
Brittleness and plasticity index of the two studied phases.

Constituent phase of the DP steel	BP [$m^{-0.5}$]	ξ
Ferrite	0.414	0.54
Martensite	1.121	0.46

$$PS = \frac{A_c}{A_g} \quad \text{Eq. (23)}$$

Here, the term h_e denotes the elastic recovery throughout the unloading and is used to correlate the PS with the work hardening rate [33].

$$h_e = h_m - h_r \quad \text{Eq. (24)}$$

This equation involves a new factor, contact radius, which is expressed in terms of $h_m - h_r$. Fig. 11 depicts the correlation between the PS and the $\frac{h_e}{h_m}$ ratio for ferrite and martensite at varying degrees of ductility. Based on Pham et al.'s work [41], the relationship between $\frac{h_e}{h_m}$ and PS can be modeled using the power law, as described by Eq. (25) [40]:

$$\left(\frac{h_e}{h_m}\right) = \alpha \cdot \left(\frac{A_c}{A_g}\right)^{\theta} \quad \text{Eq. (25)}$$

In this equation, α and θ are the constants in the power-law equation, and the results are presented in Fig. 12. To prevent potential anomalies, four separate areas were analyzed for each phase. Considering $\frac{A_c}{A_g} = 1$ as the threshold between sink-in and pile-up, both ferrite and martensite exhibited pile-up based on the relative variations in their loading–unloading height differences and changes in their two measured areas. This finding is consistent with the inferences of previous studies [17, 46]; moreover, the AFM images in Fig. 10 confirm that pile-up occurred in regions adjacent to the nanoindentation sites.

3.3. Finite element analysis

To validate the elastoplastic data extracted from the nanoindentation experiments, the penetration of the Berkovich tip into each constituent phase was simulated by FEA. The friction coefficient between the indenter and the specimen surface was set to 0.2, consistent with other nanoindentation simulation studies [16,23], as this value does not inadvertently alter the results [47]. The simulation model featured a rigid indenter without plasticity, whereas the specimen was assumed to demonstrate linear elasticity and perfect plasticity. During the numerical simulation, the downward movement of the indenter along the central axis of the sample was recorded against the tip stroke. These data were then used to verify the experimentally recorded stress–strain curves. A comparison between the local and global remeshing techniques revealed that the most accurate results were obtained using the local mode with a die displacement control of 0.235 in the locally meshed zone. The simulation results indicated that the Lagrangian incremental solution analysis in the 3D domain provided better responses than the Eulerian and ALE approaches. However, this method yielded less accurate results at the initial tip–sample contact point owing to the singularities caused by excessive element distortion and relatively high round-off errors. The ALE technique improved the mesh and geometry compatibility, preventing excessive mesh damage in critical regions while maintaining the kinetic energy constraints. Two criteria were employed to validate the calculated nanoindentation-based flow data: First, a semiquantitative comparison of the indented area obtained by FEA with the AFM profile of the projected zone; second, a quantitative comparison between the load–displacement curves derived from the simulations and nanoindentation experiments. Fundamentally, the stress–strain data extracted from the nanoindentation tests were incorporated into the FEA model to accurately simulate the load–displacement curves of both the phases of the studied DP steel. In the FEA model, the force response history was plotted against the tip displacement, and the plot was compared with the main experimental loading curve. To ensure that the simulation results were independent of the mesh, the load in the tip contact zone was monitored to evaluate the required

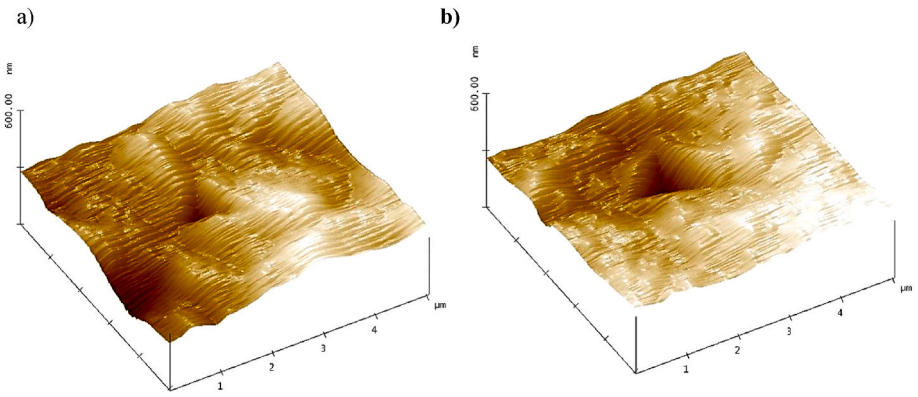

Fig. 10. AFM images of (a) martensite and (b) ferrite, acquired by instrumental nanoindentation.

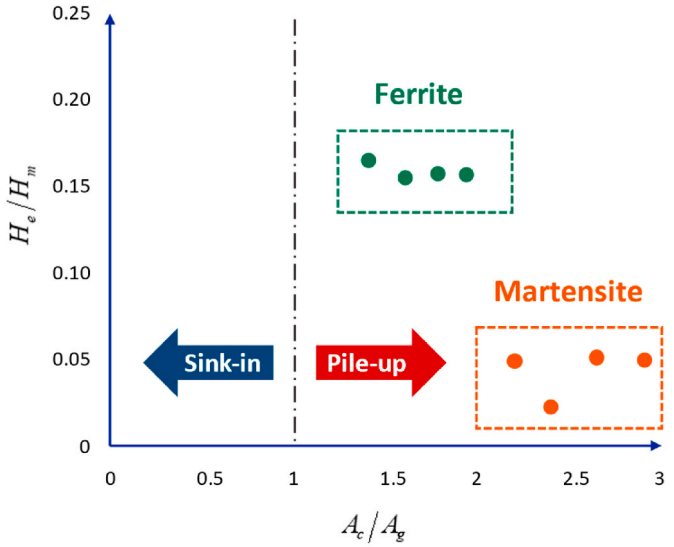

Fig. 11. Relationship between the A_c/A_g and h_e/h_m ratios for ferrite and martensite.

number of elements. Generally, large strain gradients or high stress concentrations in regions of restricted deformation could not be accurately captured using large element sizes owing to insufficient integration points. Since the simulation results did not vary when more than 12, 000 elements were implemented, this value was selected for the subsequent FEA simulations to guarantee reliability of the results for both the constituent phases. Fig. 12 shows the stress contours within the indented areas of both the phases, obtained from the projected areas in the FEA model and the AFM profiles.

The length and the profile of the indented zone showed good agreement, confirming the accuracy of the nanoindentation-based calculations incorporated into the preprocessing step of the FEA simulation. Fig. 12 indicates that the stress values near the tip were higher in martensite than those in ferrite. Although the indented areas exhibited similar patterns after the indentation, the material flow near the tip reveals that martensite experiences stronger work hardening.

In both ferrite and martensite, the maximum stress occurred near the edges of the pyramidal tip, leading to local yielding at these contact points due to the stress incompatibility between the adjacent sections. This local yielding is attributed to the geometry of the Berkovich tip, which rendered the central section less resistant to penetration and generated a nonuniform stress distribution near the tip.

Moreover, the occurrence of pile-up near the indenter tip during the loading phase was evidenced by both the AFM and FEA results, indicating local plastic deformation. Fig. 13 presents the pile-up patterns of ferrite and martensite, obtained from the AFM and FEA results. The pile-up pattern was more pronounced in the central zone of the nanoindentation field than in other regions (see Fig. 14).

The results indicate that both phases exhibited elastoplastic behavior during loading, followed by partial elastic recovery during unloading. Additionally, the material at the neighboring margins of the indentation experienced less plastic deformation owing to the diminishment of the horizontal component of the indenter load. Consequently, the pile-up at the margins of the indenter was more profound than that in other regions. Although the pile-up height on the facet side was smaller than the actual height, this discrepancy is acceptable, relative to the total indentation depth. The strong agreement between the FEA and nanoindentation data suggests that the results of the nanomechanical evaluation and FEA were consistent. By monitoring the vertical displacement of a specific node beneath the tip, the force applied to that node was measured accurately. The results exhibited slight inconsistencies because the average radius of curvature of the indenter tip was approximately 200 nm, arising from errors due to manufacturing that reduce the tip sensitivity. At the onset of indentation, the maximum stress beneath the tip exceeded the yield strength of both ferrite and martensite, indicating that plastic deformation occurred near the tip immediately upon contact. During unloading, the elastic deformation gradually diminished to zero; hence, the final indentation comprised the residual plastic deformation alone. The consistency in the hardness values determined by the nanoindentation experiments and FEA, along with the load–displacement history and the indented area, demonstrates the accuracy of the proposed model in predicting the stress–strain curve from nanoindentation data. Table 8 listed the characteristic points of FEM-derived load-displacement curve to be validated with experimental curve of instrumental nanoindentation. As can be inferred, good accordance between experimental and FEM data validated the suggested workflow in this research.

For caculation of fracture thoughness form naoindentation data, the maximum force (P) was used in addition to geometrical parameters recorded from AFM topography (crack length at edges and central triangle dimenstion as sum of them both) that have to be implemented in Eq. (19) and Eq. (20) and results were listed in Table 6. Through FEM simulation, the countour plot illustrated in Fig. 12 yield the similar projected area and length/crack-like lines that can be consequently used for estimation of acreage fracture thoughness. For plasticity index, the experimental areas of the plastic and elastic deformation sections was easily recorded by AFM topological scheme and their relative fraction was then labelled as ξ. For FEM simulation by ABAQUS software, the A_1 and A_2 values was accurately measured by point-tracking utility option in field output and connecting integral points of all involved elements in the indented area. Table 9 listed the experimental and AFM-mapped fracture thoughness and plasticity index for both phases. The comparasion between data shows acceptable accuracy of FEM simulation for both parameters. The key causes of such discrepensies in FEM results are

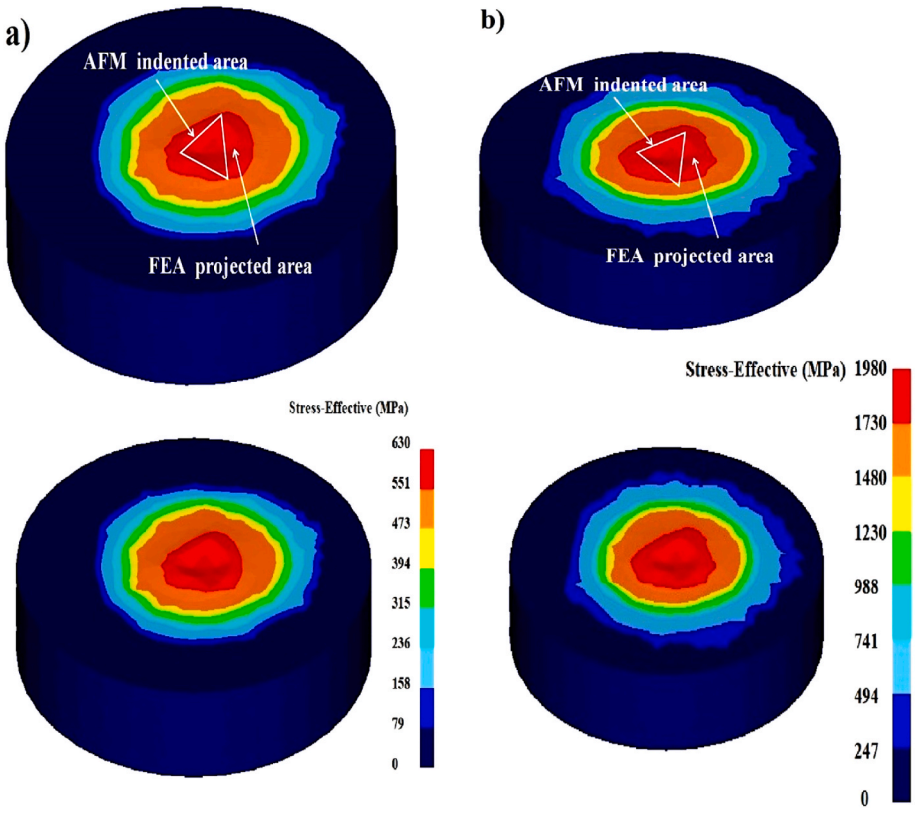

Fig. 12. Stress contours within the indented areas of the (a) ferrite and (b) martensite phases, obtained from FEA analysis and AFM mapping.

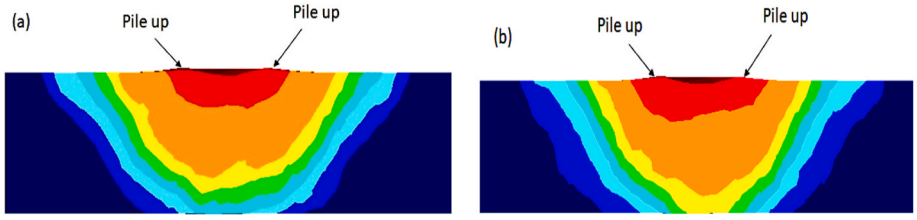

Fig. 13. Pile-up in (a) ferrite and(b) martensite after nanoindentation.

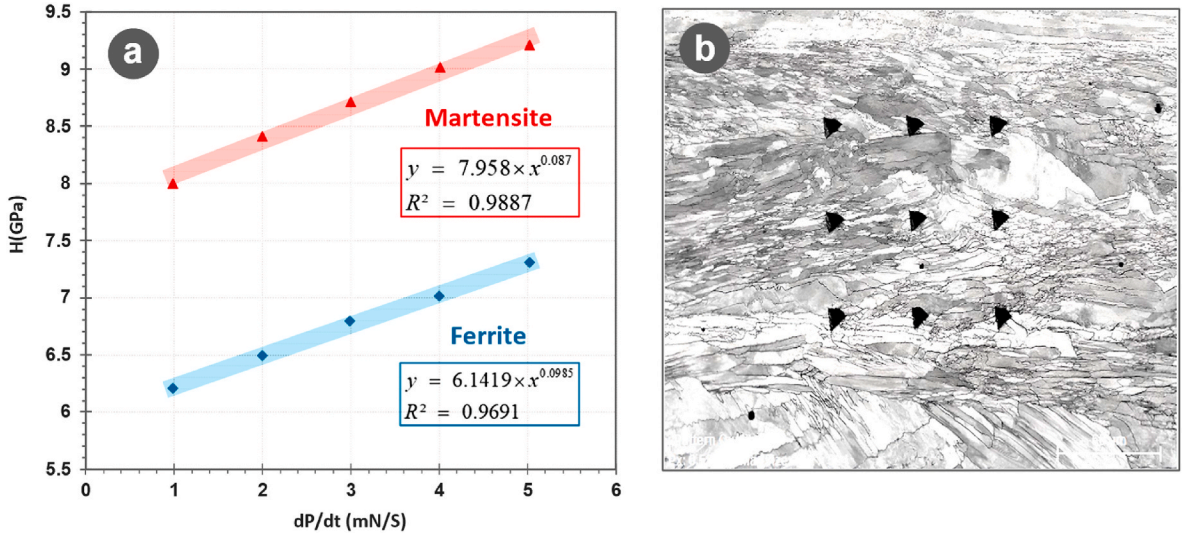

Fig. 14. (a) Variation in the hardness (H) of ferrite and martensite with the loading rate ($\frac{dP}{dt}$)and (b) SEM image of the indented area in the heat-treated DP steel.

Table 8
Validation of FEM-derived results with instrumental nanoindentation data.

Parameter	Unit	Experimental data	FEM simulation
Maximum load (ferrite)	μN	2760	2711
Maximum load (martensite)	μN	3078	3098
Maximum depth (ferrite)	Nm	185	194
Maximum depth (martensite)	Nm	76	88
Residual depth (ferrite)	Nm	104	94
Residual depth (martensite)	nm	44	50
Projected area (ferrite)	μm^2	3.645	4.102
Projected area (martensite)	μm^2	2.17	2.23

Table 9
Validation of fracture thoughness and plasticity index extracted from FEM.

Parameter	Unit	AFM data	FEM simulation
Average K_{IC} (ferrite)	MPa ($m^{0.5}$)	20.5	22
Average K_{IC} (martensite)	MPa ($m^{0.5}$)	9.2	10.2
Palsticity index (ferrite)	–	0.54	0.52
Plasticity index (martensite)	–	0.46	0.4

discretization errors in projected and indented area, formulation errors, and numerical mistakes in defining boundaries of indented are. Discretization errors comes from approximating a continuous indented triangle with a discrete mesh-based borders while numerical errors stem from the computational process such as round-off and truncation errors.

3.4. Strain-rate sensitivity

Strain-rate sensitivity (SRS) is an important material property for understanding thermally activated plastic deformation under an applied stress, such as creep. For most engineered metals and alloys, the SRS ranges from 0 to 0.1 and increases with the temperature. For superplastic materials, the SRS can reach 0.33 or greater. This parameter can be determined by uniaxial tension or compression tests. Considering the growing interest in evaluating the SRS of nanocrystalline materials and thin films, nanoindentation methods are widely implemented to ensure accurate calculations. Lucas and Oliver developed a technique to determine the SRS by measuring the hardness at different strain rates. While their method is effective for moderate to high strain rates, it faces challenges at low strain rates because of thermal drift, which affects the indenter displacement. As previously mentioned, hardness can be determined from Eq. (4), and SRS can be calculated by power law using Eq. (26), which is applicable for materials subjected to creep that obey the power law in the absence of any elastic contribution [48]:

$$H = B \cdot \left(\frac{dP}{dt}\right)^m \quad \text{Eq. (26)}$$

In this equation, B is a constant, (dP/dt) represents the loading rate, and m denotes the SRS. When m is positive, an increase in the loading rate (dP/dt) is expected to increase the hardness. Previous studies have shown that initiating the test at a higher loading rate and concluding it at a lower rate reduces the thermal drift. Research findings indicate that m decreases slightly with decreasing indentation depth. Moreover, m value decreases with increasing hardness, regardless of whether the hardness increase is due to plastic deformation in different samples or variations in indentation size of the same sample. Fig. 15(b) displays a backscattered electron SEM image of a 3 × 3 indentation matrix on the surface of the heat-treated DP steel, highlighting different locations within the ferrite and martensite phases. Indentations were performed at various loading rates, resulting in different dimensions of the projected areas due to the varying hardness values of the indented regions. Fig. 15 (b)demonstrates that the indentation sizes were smaller than the distances between the indents, thereby confirming that the indents did not influence each other. As shown in Fig. 15(a), the calculated m value of the ferrite phase, with a lower hardness and a greater indentation depth, was 0.0985, whereas that of the martensite phase was 0.087. Generally, materials with greater m values exhibit better deformability and ductility. The calculated m values of the martensite and ferrite phases, representing their brittle and ductile nature, respectively, concur with the results of a previous study [42].

Fig. 15 (a) shows bright-field TEM images of the interstitially annealed heat-treated DP steel samples. Many geometrically necessary dislocations (GND) were formed in the ferrite grains and ferrite–martensite interracial zones because of the volume change by 2 %–4 % during the austenite–martensite transformation to accommodate the plastic strain gradients in the crystal Fig. 15(b) reveals high-dislocation-density regions that were pinned by numerous fine iron carbide particles; however, GNDs are considered to be mobile and can lead to continuous yield stress in DP steels. These mobile unpinned dislocations at the ferrite–martensite interface could either interact with each other and annihilate, or glide to the interior of the ferrite and interact with the pinned dislocations during the deformation [35]. The tangled GND substructures located within the ferrite phase obtained by annealing at a lower intercortical annealing temperature demonstrated higher line densities than those within the ferrite phase obtained by annealing at a higher temperature, owing to the occurrence of dislocation cell formation and subsequent subdrains. This fact was confirmed by previous research [37] as the formation of cells or microbands within the ferrite which are lower energy dislocation substructures. The magnitude of

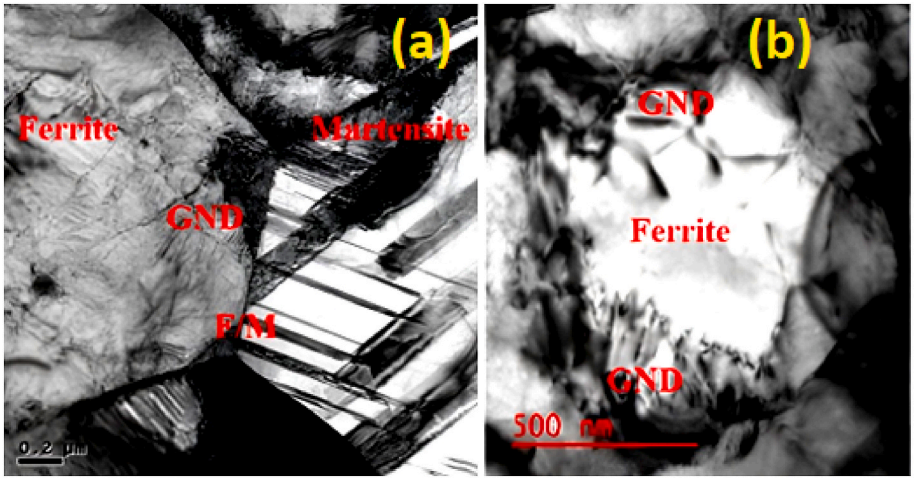

Fig. 15. TEM images of the ferrite–martensite interface consisting of interfacial GND dislocations (rearranged and partially annihilated).

subgrain disorientation and subgrain strengthening and the spacing within the internal structures of the subgrains have no considerable effect on the flow stress, rather the spacing between the subgrain boundaries governs the stress–strain response of the ferrite phase. The flow stress in ferrite during monotonic deformation can be interpreted as follows: The number of GNDs and the stored energy typically increase inside the cells, in existing cell boundaries, and newly formed cell boundaries. After the cell structure is subjected to a definite strain, and sufficient GNDs are formed, the mobile and stationary dislocations establish mutual contact, forming dislocation dipoles. Such dipoles are formed when edge or screw dislocations with opposite get rearranged within their surroundings and, under certain conditions, annihilate each other. The collapse of dislocation dipoles governs the growth kinetics of the tangled dislocation network. The kinetics of dipole collapse can be assessed using rate equation, Eq. (27) [43]:

$$\frac{dg}{dt} = -g.v_g \quad \text{Eq. (27)}$$

where g represents the dipole density and v_g is the frequency of dipole collapse when climb and cross-slip are considered as the rate-controlling mechanisms for the substructure. Such dipole collapses that occur in the forest dislocation are reciprocally related to the dislocation density inside the cell. Moreover, a higher GND density was observed inside the ferrite near the interface, and the GND density decreased upon moving away from the ferrite–martensite interface toward the center of ferrite. Such GND variations induce a stress field ramp near the interface of the two phases toward the center of ferrite. Long-range stresses in ferrite stimulate the dislocations to attain low-energy configurations by forming walls of dislocations inside a grain. Consequently, the grain gets divided into many smaller sections, forming subgrains. These results are in accordance with those of previous studies shows that the dislocation distribution in the ferrite phase is relatively heterogeneous and that its density reaches the maximum at the ferrite–martensite interface [8].

4. Molecular dynamics simulation results

The load–displacement curves of the martensite and ferrite phases, obtained via the MD simulation of the nanoindentation test, are plotted in Fig. 16 to compare their behaviors. The indenter radius was 10 Å, and the indentation velocity was set to 0.10 ($\frac{\text{Å}}{ps}$).The martensite phase experienced negative force in the loading curve when the indenter was within the proximity of the sample, and then it gradually decreased in the z-direction. This negative force signifies the adsorption force between the sample and the indenter within a specific distance. In both the phases, the indentation depth was set equal to indenter radius, i.e., 10 Å. As shown in Fig. 16, the indentation depth in both phases were the same because the MD simulation was conducted in the displacement control mode. Therefore, the difference between the hardness values of the ferrite and martensite phases is attributed to the maximum force experienced by each phase at the maximum indentation depth. According to the load–displacement curves in Fig. 16, the martensite and ferrite phases experienced maximum forces of 711and 161 nN, respectively. Thus, the martensite phase is expected to exhibit a much higher hardness than the ferrite phase.

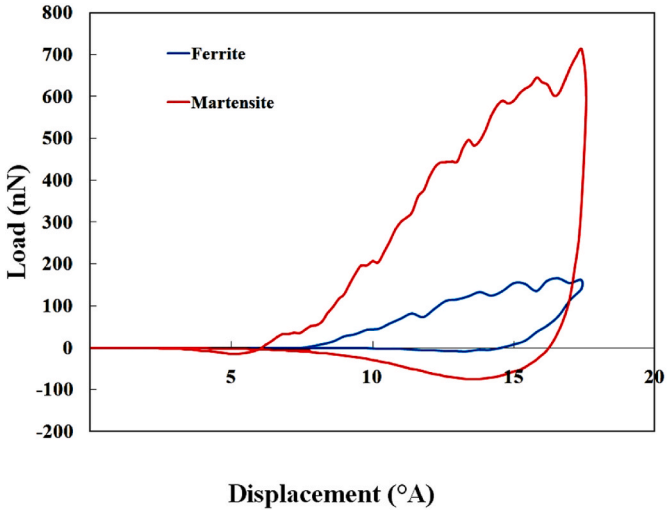

Fig. 16. Load–displacement curves of the ferrite and martensite phases.

The hardness and Young's moduli of both the phases can be determined using the Oliver–Pharr method [28], Eq. (13), and Eq. (28)–(32). In this method, the contact area (A_c) is a crucial parameter for assessing the material properties during nanoindentation [24,29].The parameters in Eq. (28)–(32) are listed and described in Table 10.

$$S = \left(\frac{dP}{dh}\right)_{h=h_{max}} \quad \text{Eq. (28)}$$

$$\frac{1}{E_r} = \frac{1-\nu_i^2}{E_i} + \frac{1-\nu^2}{E} \quad \text{Eq. (29)}$$

$$E_r = \frac{\sqrt{\pi}}{2\beta}\frac{S}{\sqrt{A_c}} \quad \text{Eq. (30)}$$

$$A_c = \pi\,(2R - h_c)\,h_c \quad \text{Eq. (31)}$$

$$h_c = h_{max} - \varepsilon\,\frac{Pmax}{S} \quad \text{Eq. (32)}$$

The amount of hardness and Young's modulus of ferrite were calculated as 7.5 and 210 GPa, respectively, whereas those of martensite were correspondingly determined as 10 and 215 GPa from the MD nanoindentation simulation; the values are in accordance with those listed in Table 5. However, MD methods face certain limitations in evaluating the properties of materials with microstructural complexities because the testing area is highly localized. Therefore, the greater difference between the hardness values of the ferrite and martensite phases, as recorded in Fig. 16, relative to those measured in the nanoindentation experiments is reasonable. In addition, implementing the Oliver–Pharr method in the nanoindentation simulation overestimated the hardness values and the Young's moduli because the material exhibited a piling-up behavior (Fig. 18). Fig. 17 displays the atomic positions in the zy and xy planes of the ferrite and martensite phases of the MD-simulated samples. The maximum indentation depth in both the sliced samples was 10 Å, and the diameter of the projected area of the indenter at maximum indentation equaled 20 Å. Because the indentation test was conducted in the displacement control mode, the projected areas in both the phases were the same, whereas the hardness varied with the force experienced at maximum indentation depth. Furthermore, a little pile-up was observed around the indenter, as visualized in Fig. 13, which deviated the hardness values and Young's modulus of ferrite and martensite calculated by the MD simulation, relative to the values listed in Table 5.

Table 10
Parameters used in Eq. (28)–(32) for nanomechanical calculation.

Parameter	Description
S	Contact stiffness in the unloading curve at h_{max}
h_{max}	Maximum displacement
E_i	1141 GPa (Young's modulus of the diamond indenter)
A_c	Projected contact area
h_c	Projected contact depth
R	Indenter radius
β	1 (A geometric constant of the indenter)
ν_i	0.11 (Poisson's ratio of the diamond indenter)
ν	0.3 (Poisson's ratio of the ferrite and martensite phases)
E	0.75 (for a spherical indenter)

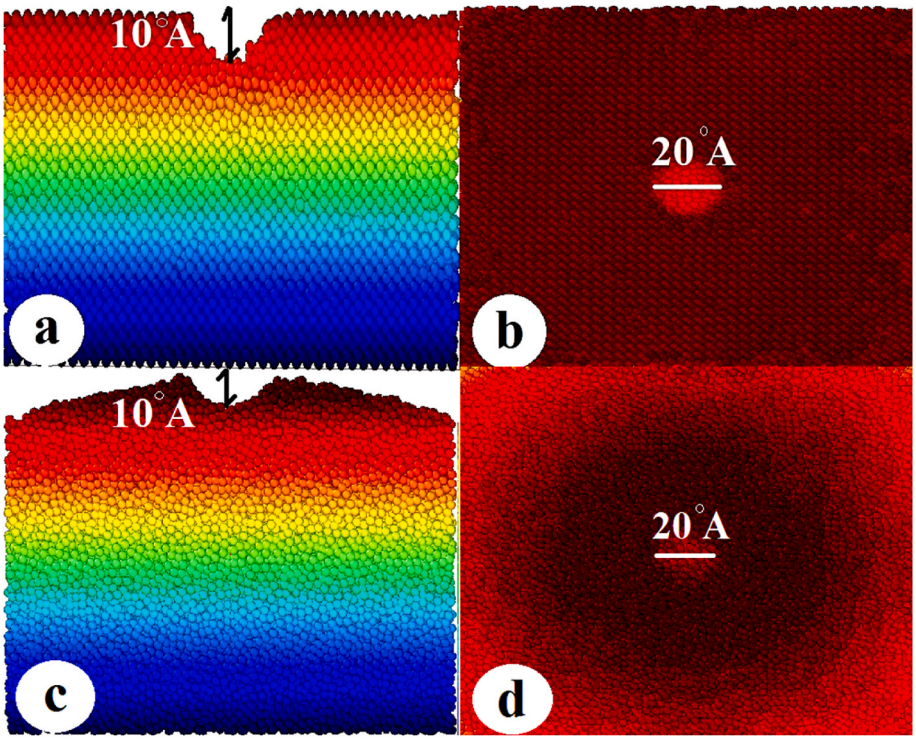

Fig. 17. Atomic positions in the zy and xy cross sections of the (a,b) ferrite and (c,d)martensite phases of the MD-simulated samples at maximum indentation depth.

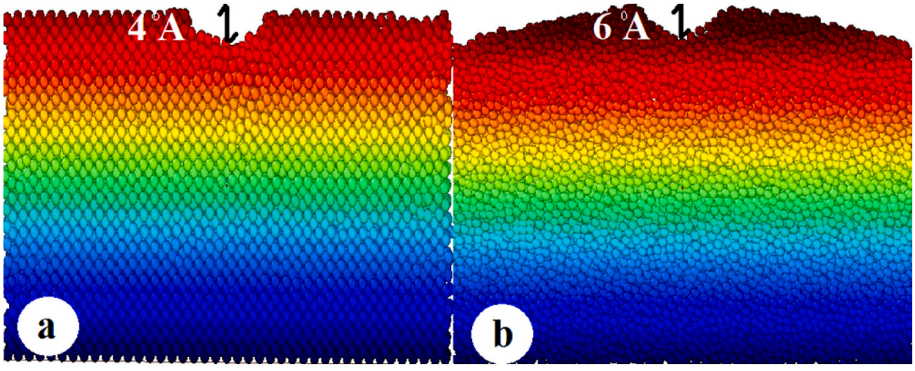

Fig. 18. Atomic positions in the zy cross section of the (a) ferrite and (b) martensite phases of the MD-simulated samples after unloading.

Fig. 16 shows that during unloading, while the indentation load approached zero because of plastic deformation and exhibited residual indentation, the displacement did not converge into the origin. Fig. 18reveals that the residual indentation depths after unloading were 4 and 6 Å for ferrite and martensite, respectively, which agree with the values in Fig. 16.

Application of load by the indenter into the substrate during the nanoindentation test exerts stress on the atoms beneath and around the

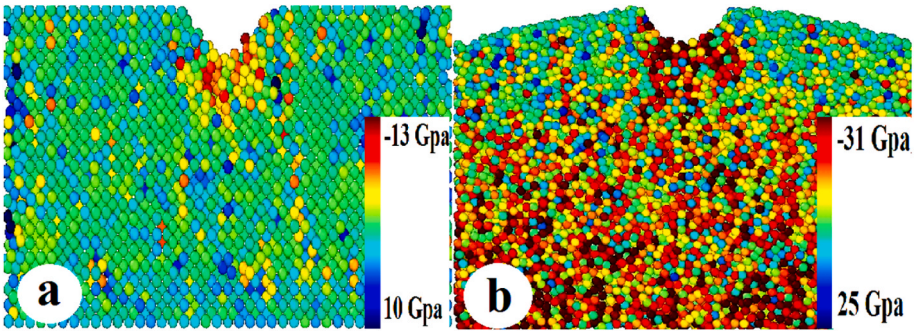

Fig. 19. Stress distribution of the atoms in the zy cross section of the (a) ferrite and (b) martensite phases of the MD-simulated samples at maximum indentation depth.

indenter. Hence, a nonuniform stress distribution is expected throughout the sample. Because of the localized pressure exerted by an indenter during its penetration into a material, a high von Mises stress concentration occurs around the indenter [44]. Fig. 19(b)reveals that the atoms around the indenter in the martensite phase experienced a higher compression stress than those in the ferrite phase (Fig. 19(a)), which are marked in red color. The maximum compression stresses on the martensite and ferrite atoms in their respective indentation zones were −31 and −13 GPa, which are in good agreement with the values in Fig. 16. In addition, more atoms in the martensite phase experienced compression stress beneath the indentation zone because the total stress on martensite was higher than that on ferrite. Therefore, the martensite phase exhibited greater hardness and BP values, as mentioned in Table 7.

5. Conclusion

In this study, a hybrid experimental–numerical nanomechanical approach was implemented to determine the stress–strain correlation of the constituent phases of DP steels with ferrite–martensite microstructures. The following inferences are drawn based on the obtained results.

1. The FEA and MD calculations were performed efficiently. The load–displacement curves, the hardness values, and Young's modulus of each phase were determined with a considerable accuracy. The values computed using the experimental and numerical approaches exhibited good agreement.
   2.The methodology of this study can be employed for analyzing the flow curves, ductility, and fracture toughness of alloys with composite-like microstructures as well as multiphase materials and composite structures. The geometric features of the interphase boundaries with respect to the dislocations significantly affected the microstructure–microplasticity relationship and the cell formation kinetics.
3. Constitutive equations and nanoindentation data at various strain rates were used to extract SRS of each phase and its variation with hardness, using the nanoindentation.
4. Nanomechanical parameters such as the elastic modulus, yield stress, hardness, flow properties, and fracture behavior (K_c-PB-ξ) of both phases of the DP steel were investigated, and the basic micromechanical deformation mechanisms were correlated with each other to compare either the work hardening and plasticity behaviors.
5. The MD simulation results indicate that the work hardening exponent was higher for martensite than for ferrite, owing to the presence of non-annihilated GNDs that stimulate the work hardening mechanism.

Declaration of competing interest

The authors declare that they have no known competing financial interests or personal relationships that could have appeared to influence the work reported in this paper.

References

[1] Tasan CC, Diehl M, Yan D, Bechtold M, Roters F, Schemmann L, Zheng C, Peranio N, Ponge D, Koyama M. Annu Rev Mater Res 2015;45:391–431.
[2] Niu G, Ding C, Liu Z, Jia X, Chen H, Gong N, Wang Y, Cheh DTC, Misra R, Wu H. Mater Sci Eng, A 2024;892:146072.
[3] Jamei F, Mirzadeh H, Zamani M. Mater Sci Eng, A 2019;750:125–31.
[4] Alibeyki M, Mirzadeh H, Najafi M, Kalhor A. J Mater Eng Perform 2017;26:2683–8.
[5] Ma C, Yan X, Gernay T. Eng Struct 2023;288:116256.
[6] Tang A, Liu H, Chen R, Liu G, Lai Q, Zhong Y, Wang L, Wang J, Lu Q, Shen Y. Int J Plast 2021;137:102920.
[7] Wang J, Li W, Zhu X, Zhang L. Mater Sci Eng, A 2022;832:142424.
[8] Ghassemi-Armaki H, Maaß R, Bhat SP, Sriram S, Greer JR, Kumar KS. Acta Mater 2014;62:197–211.
[9] Ghassemi-Armaki H, Chen RP, Maruyama K, Yoshizawa M, Igarashi M. Mater Lett 2009;63:2423–5.
[10] Park M-h, Matsubayashi R, Shibata A, Tsuji N. Mater Sci Eng, A 2024;918:147445.
[11] Dai Z, Ding R, Yang Z, Zhang C, Chen H. Acta Mater 2018;144:666–78.
[12] Zhang H, Sun M, Liu Y, Ma D, Xu B, Huang M, Li D, Li Y. Acta Mater 2021;211:116878.
[13] de la Concepción VL, Lorusso HN, Svoboda HG. Procedia Materials Science 2015;8:1047–56.
[14] Paul SK. Mater Des 2013;44:397–406.
[15] Jahanara AH, Mazaheri Y, Sheikhi M. Mater Sci Eng, A 2019;764:138206.
[16] Wu-Rong W, Chang-Wei H, Zhong-Hua Z, Xi-cheng W. Mater Des 2011;32:3320–7.
[17] Vafaeenezhad H, Aliakbari-Sani S, Seyedein SH, Ghosh A, Eivani AR. J Mater Res Technol 2022;18:4617–30.
[18] Vafaeenezhad H, Aliakbari-Sani S, Kalaki A, Ebrahimi GR, Hirsch J. J Magnesium Alloys 2024;12:3370–93.
[19] Long X, Shen Z, Li J, Dong R, Liu M, Su Y, Chen C. J Mater Res Technol 2024;29:2437–47.
[20] Tao P, Huang S, Long Z, Deng Z, Zhu X, Xu X, Deng H, Yang Y. J Alloys Compd 2024;999:174983.
[21] Tanaka Y, Hattori K, Harada Y. Mater Char 2022;190:112055.
[22] Long X, Li Y, Shen Z, Su Y, Gu T, Siow KS. J Manuf Process 2024;131:1897–916.
[23] Fauvel V, Gaillard Y, Guillemet R, Garabédian P, Richard F. Int J Mech Sci 2023;245:108091.
[24] Patra L, Pandey R. Mater Today Commun 2022;31:103623.
[25] Alibeyki M, Mirzadeh H, Najafi M. Vacuum 2018;155:147–52.
[26] Bhadeshia HKDH, Honeycombe RWK. Steels: structure, properties, and design. Elsevier; 2024.
[27] Doan D-Q. Mater Chem Phys 2022;291:126725.
[28] Xu S, Wan Q, Sha Z, Liu Z. Comput Mater Sci 2015;110:247–53.
[29] Feng C, Peng X, Fu T, Zhao Y, Huang C, Wang Z. Phys E Low-dimens Syst Nanostruct 2017;87:213–9.
[30] Lv J, Bai M, Cui W, Li X. Nanoscale Res Lett 2011;6:200.
[31] Mayo SL, Olafson BD, Goddard WA. J Phys Chem 1990;94:8897–909.
[32] Veiga RGA, Becquart CS, Perez M. Comput Mater Sci 2014;82:118–21.
[33] Fischer-Cripps AC. Introduction to contact mechanics. Springer; 2007.
[34] Zamiri A, De S. J Mech Behav Biomed Mater 2011;4:146–52.
[35] Paul SK. Journal of Alloys and Metallurgical Systems 2025:100153.
[36] Giannakopoulos A, Suresh S. Scr Mater 1999;40:1191–8.
[37] Paul SK, Stanford N, Hilditch T. Mater Sci Eng, A 2015;638:296–304.
[38] Lawn B, Marshall D. J Am Ceram Soc 1979;62:347–50.
[39] Anstis G, Chantikul P, Lawn BR, Marshall D. J Am Ceram Soc 1981;64:533–8.
[40] Xu Z-H, Ågren J. Philos Mag 2004;84:2367–80.
[41] Pham T-H, Nguyen N-V. Constr Build Mater 2021;268:121211.
[42] Cao B, Iwamoto T. Steel Res Int 2017;88:1700022.
[43] Eisenlohr P, Blum W. Mater Sci Eng, A 2005;400:175–81.
[44] Muthupandi G, Lim KR, Na Y-S, Park J, Lee D, Kim H, Park S, Choi YS. Mater Sci Eng, A 2017;696:146–54.